Article

Photoluminescence Investigations and Band Gap Engineering in Environment Friendly ZnO Nanorods: Enhanced Water Treatment Application and Defect Model

Sumit Kumar, Jyoti Pandey, Ritika Tripathi, and Suchitra Rajput Chauhan*

Read Online

ACCESS | Metrics & More | Article Recommendations

ABSTRACT: The inadvertent discharge of industrial effluents, mainly textile, contributes to the complex contamination load in water bodies. Textile dyes are the critical effluents and recalcitrant to traditional remediation procedures. Therefore, energy viable and environment friendly solutions are needed. In this study, we have synthesized zinc oxide nanorods (NRs) at various temperatures using modified thermal decomposition and evaluated its photocatalytic activities. Field effect scanning electron microscopy has confirmed rod-like morphology till T_S = 500 °C and spherical morphology from T_S = 600 °C onward. Photoluminescence spectra have shown a prominent defect peak in the synthesized ZnO, except for the NRs synthesized at 300 °C. Synthesized ZnO NRs and NPs have been employed to degrade crystal violet (CV) and congo red (CR) dyes. ZnO NRs have shown impressive photocatalytic performance with faster treatment time as compared to the earlier reports. Synthesis parameters are well correlated with the observed high efficiency and the band gap tailoring. Based on our findings, for the first time, we have proposed (i) defect model correlating synthesis parameters with defect states, (ii) systematic correlation of defect states with photocatalytic efficiency, and (iii) ZnO nanorods synthesized at 300 °C via an improved synthesis method as a promising photocatalytic solution to degrade the CV and CR dyes in contaminated water.
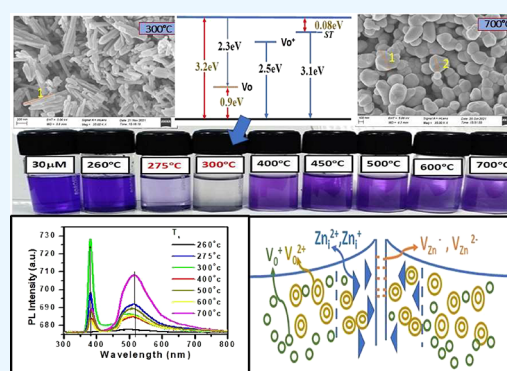
1. INTRODUCTION

Textile industries, since their inception, have been discharging hazardous effluents and dyes into the water bodies through different channels. A global survey has indicated a 40% deficit in water availability to meet the estimated demand by the year 2030.[1] Thus, development of better treatment technologies, techniques, and materials than conventional physiochemical treatments like adsorption, coagulation, ozonation, flocculation, and membrane filtration is needed. Conventional treatment techniques either fail to completely demineralize the effluents[2−4] or generate other waste products. Among all techniques for textile wastewater (TWW) remediation, the semiconductor nanomaterial-based photocatalysis being environment friendly is a plausible technology.[5] Soon, photocatalysts would be in the spotlight to remediate TWW due to their solitary capability of breaking larger textile dye molecules into smaller molecules and harmless byproducts via the environment friendly route. In addition, photocatalysts utilize photogenerated electrons and holes[6] to degrade effluents, so it is a clean and low-cost technique to combat these problems. ZnO is well known due to its impressive benefits including green properties, good chemical stability, biocompatibility, distinct electronic structure, and low production cost, thus becoming an obvious choice in photocatalytic fields.[5] Nano

ZnO due to its human friendly nature[7] becomes a potential candidate for its utility in the wastewater treatment via photocatalysis.

When the ZnO photocatalyst is exposed with suitable radiations, it populates e^-(s) and hole(s) in the CB and VB, respectively. This initiates redox reaction with water and oxygen resulting in generation of reactive oxygen species (ROS), which in turn degrade dyes or organic effluents into CO_2 and minerals.[8] An avid recombination of these photogenerated carriers is invariably detrimental to quantum efficiency of the photocatalyst to degrade dye molecules.[9−13] Solid surface adsorbed gases, segregated impurities, and defects are sources/sinks of photogeneration carriers. Therefore, control of defects and associated band tailoring is of paramount importance for enhanced photocatalytic activity of ZnO.
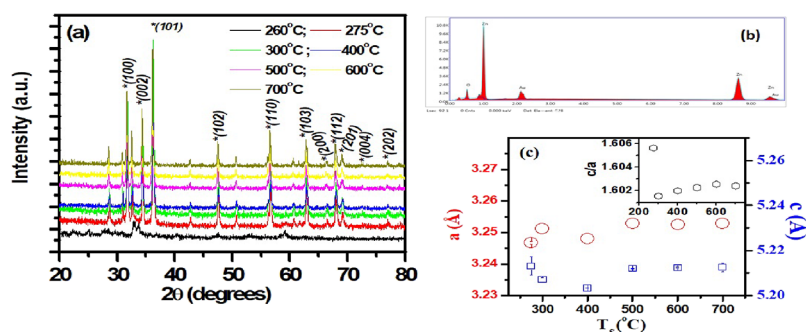
Figure 1. (a) X-ray diffraction pattern of the MSMATD synthesized ZnO nanomaterial. The sample prepared at 260 °C did not show the formation of the ZnO phase. The peaks observed in the diffraction pattern were identified as the ZnO wurtzite phase in samples synthesized at T_S = 275−700 °C. (b) EDX spectrum of ZnO prepared at 300 °C. (c) Lattice parameters obtained from the indexing and refining program using XRD data.

A rigorous literature survey indicates that there are no reports on the detailed XRD and photoluminescence investigation of ZnO synthesized over a wide range of temperature. There are number of legitimate motives for such systematic investigation and its correlation with photocatalytic efficiency. In this study, we have developed an improved and environment friendly synthesis approach, magnetic stirred-mechanical assisted thermal decomposition. We have undertaken synthesis parameters, for instance, synthesis temperature, and post-synthesis treatments for realizing band gap engineering through the control of defects and surface states. Also, the findings of our work establish the role of defects in reducing degradation time of crystal violet and congo red dyes.

2. EXPERIMENTAL DETAILS

Zinc acetate dihydrate is a preferred choice as a precursor for the synthesis of ZnO nanomaterials pertaining to its low decomposition temperature.

2.1. Synthesis: Magnetic Stirred Mechanical-Assisted Thermal Decomposition (MSMATD) Method. Zinc acetate was manually ground for 1 h and then heat-treated at the desired temperature in the range from 260 to 700 °C (T_S) for 4 h followed by quenching to room temperature. The samples that were heat-treated at $T_S \geq 500$ °C were quenched to room temperature (RT) in air from 425 °C, and samples heat-treated at $T_S < 500$ °C were air-quenched from T_S to RT. Obtained samples were crushed in a mortar and pestle for 2 min and then magnetically stirred in deionized (DI) water (volume used = weight of powder × 10) for a 1 h duration. Stirred mixtures were then filtered using Whatman filter paper to obtain the solid powders followed by their drying at 70 °C for 8−10 h.

2.2. Characterizations. X-ray diffraction analysis confirmed the crystallographic phase of the synthesized material. The theta−theta powder X-ray diffraction method (Panalytical EMPYREAN) was adopted to obtain the X-ray diffraction pattern. Diffraction intensity was recorded at 45 kV applied voltage and 45 mA current setting. The diffraction pattern was recorded for 2θ between 20 and 80°. Lattice parameters were determined via PowderX software.[14] Particle size of the synthesized ZnO nanomaterials was determined from X-ray diffraction data via the Williamson−Hall plot. Morphology and particle size of the synthesized samples were determined by field effect scanning electron microscopy (FE-SEM, Sigma-300, Carl Zeiss), and elemental composition was determined by energy-dispersive X-ray spectroscopy (EDX). The band gap was determined using diffuse reflectance spectroscopy and, a decrease in the concentration of dye solutions was determined by UV−visible spectroscopy (Lambda-365, PerkinElmer). A Witech Alpha 300 RAS system was employed to record the photoluminescence emission spectrum at λ = 355 nm and 285 μW incident power. An emission signal was recorded using a charge coupled detector.

2.3. Photocatalytic Testing of ZnO Nanomaterial Synthesized via MSMATD against the Crystal Violet (CV) Dye and Congo Red (CR) Dye. *2.3.1. Dye Solution.* Various dye solutions of different molarities using CV and CR dyes and DI water were prepared for photocatalytic testing. Here, the preparation method for one dye solution (CV, 10 μM solution) is described in detail. CV dye powder (1.2 mg) was added to 300 mL of DI water followed by the magnetic stirring of the resulted solution for 1 h at 250 RPM (rotations per minute) at RT.

2.3.2. Photocatalytic Testing. The synthesized ZnO photocatalyst was added to each test bottle containing 10 mL of solution in the range from 1 to 30 mg. The test bottles were exposed to the 80 W mercury lamp. The efficiency of the synthesized ZnO nanophotocatalyst was determined in terms of change in the concentration of the dye through UV−visible absorption measurements.

3. RESULTS AND DISCUSSION

3.1. X-ray Diffraction (XRD). The XRD patterns for all the samples from 275 to 700 °C show the polycrystalline ZnO phase corresponding to the wurtzite hexagonal crystal structure. Diffraction peaks due to (100), (101), (102),

Table 1. Results Obtained from XRD, FE-SEM, and DRS Analysis

| T_S (°C)	diameter (evaluated from XRD data) (nm)	based on feature indicated in FE-SEM		absorption peak position (nm)
		aspect ratio/ diameter	morphology	
275		21.8	nanorods	380.0
300		19.2	nanorods	380.0
400		9.1	nanorods	385.6
500		5.9	nanorods	386.1
600	114.5	~250 nm	nanoparticle	386.1
700	116.5	~500 nm	nanoparticle	386.1
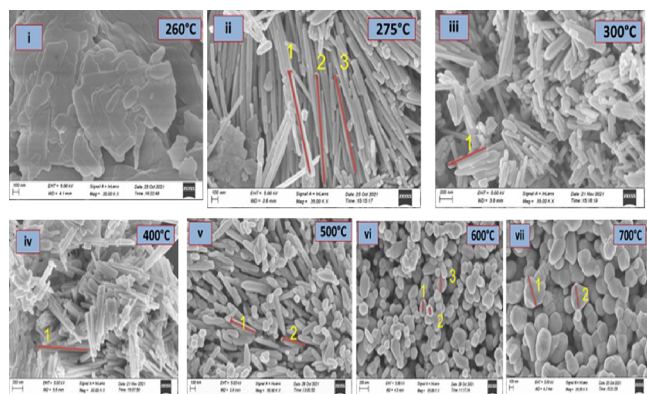
Figure 2. (i−vii) FE-SEM of ZnO prepared by the MSMATD method at 35,000× magnification. Indicated nanorods and nanoparticles have dimensions (in nm) as (ii) 1, 1368.56; 2, 1472.77; 3, 1450.65; (iii) 1020.53; (iv) 657.72; (v) 1, 595.101; 2, 521.87; (vi) 1, 252; 2, 147; 3, 204; (vii) 1, 417; 2, 501. At low temperatures, there was a growth of nanorods, whereas at elevated temperatures, a globular structure was formed.

(110), (002), (103), (112), (201), (200), (004), and (202) planes have been observed (Figure 1a). JCPDS file 36-1451 was employed for identifying the phase of the synthesized ZnO. The spurious low intensity peaks observed between 2θ = 20 and 35° could be due to impurities in the sample or intermediate product. Vijayalakshmi et al.[15] reported the presence of both zinc hydroxide and zinc oxide phases in raw ZnO powder and obtained a pure ZnO phase upon its sintering at 900 °C. Luković Golić et al.[16] prepared ZnO from zinc acetate dihydrate via the sol−gel process and observed peaks corresponding to zinc acetate, zinc oxide, and zinc hydroxide acetates (ZHA) in the synthesized powder. The authors obtained phase pure ZnO after washing the sample with methanol to remove ZHA. Malhotra et al.[17] prepared

Table 2. Results from PL Peak Fitting, Peak Position (in nm), FWHM, Area under the Curve, and Normalized Area under the Peaks with Respect to the Respective UV Peaks Are 100%

T_S (°C)	peak	FWHM	area under the peak	normalized area (in %)	E (eV)
275	382.2	13.9	356.3	100.0	3.2
	535.6	64.1	635.2	178.3	2.3
	495.7	45.4	520.4	146.1	2.5
	586.4	204.6	861.0	241.7	2.1
300	381.7	12.6	749.1	100.0	3.2
	395.4	21.8	258.0	34.4	3.1
	544.5	178.7	574.1	76.6	2.3
	500.5	80.7	792.1	105.7	2.5
400	384.6	17.2	161.5	100.0	3.2
	581.5	186.5	398.9	247.1	2.1
	540.0	66.9	291.3	180.4	2.3
	498.3	50.9	369.1	228.6	2.5
500	384.9	16.5	232.2	100.0	3.2
	534.1	64.3	525.8	226.5	2.3
	494.9	46.7	471.0	202.9	2.5
	590.2	207.3	759.7	327.2	2.1
600	383.9	15.8	132.6	100.0	3.2
	495.9	49.1	389.1	293.5	2.5
	539.5	71.0	412.1	310.8	2.3
	632.5	226.0	480.0	362.1	2.0
700	385.1	16.8	259.8	100.0	3.2
	497.2	47.6	1063.1	409.2	2.5
	535.7	67.8	1484.0	571.2	2.3
	384.9	16.5	232.2	499.0	2.1

ZnO via phytoassisted precipitation using a *Eupatorium odoratum* medicinal plant and observed peaks from intermediate products along with ZnO in the XRD pattern. Peak intensities in Figure 1a clearly indicate ZnO as the
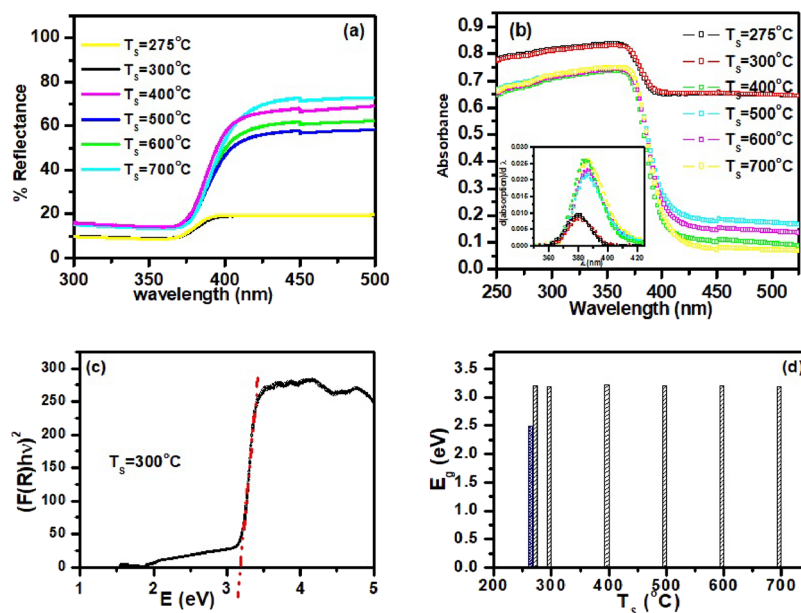

Figure 3. (a) Room temperature diffuse reflectance spectra of ZnO nanorods and nanoparticles prepared by the MSMATD method. (b) UV−visible absorption spectra of ZnO nanoparticles/nanorods prepared by MSMATD, 1 h at 275 °C ≤ T_S ≤ 700 °C. The inset shows the differential of absorbance with respect to wavelength versus wavelength indicating the peak position. Table 1 contains all peak positions. (c) Kubelka− Munk function versus energy plot for the ZnO nanorod prepared at 300 °C. Intercept of the dashed line shows the band gap. (d) Band gap values obtained for all the samples prepared by MSMATD from 275 to 700 °C as a function of synthesis temperature.
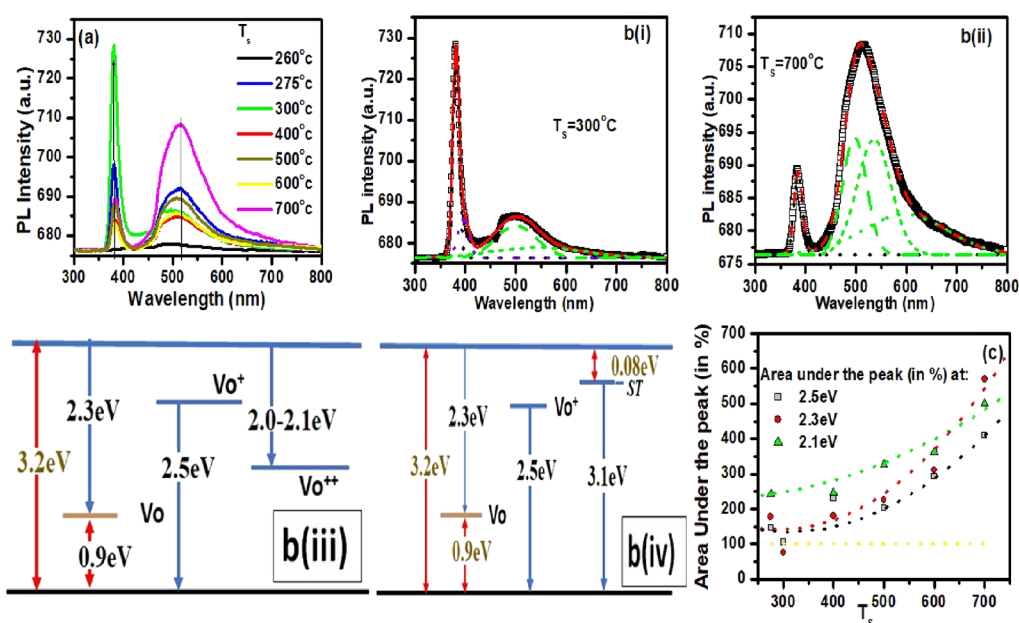
Figure 4. (a) PL spectra of ZnO nanorods and nanoparticles synthesized via the MSMATD approach at different synthesis temperatures. (b) (i, ii) Gaussian peaks fitted to a broad band in the visible region and sharp peak in the UV region for ZnO nanoparticles and nanorods prepared by MSMATD at 275 °C $\leq T_S \leq$ 700 °C (only two graphs are shown for conciseness, and the corresponding energy level diagrams are shown in panels (iii, iv)). The red line shows overall fitting, black dot curve, 3.2 eV peak; green dash curve, 2.5 eV peak; green color short dash curve, 2.3 eV peak; green dot curve, 2.1 eV peak; violet dot curve, 3.14 eV peak. (iii) Various transition states of ZnO NRs and NPs synthesized at 275, 400, 500, 600, and 700 °C. (iv) Various transition states of ZnO NRs synthesized at 300 °C, ST, surface traps. (c) Observed PL intensities corresponding to 2.1, 2.3, and 2.5 eV peaks from MSMATD synthesized nanorods and nanoparticles over 275−700 °C. The yellow dotted line indicates the normalized area under the PL peak in the UV range.
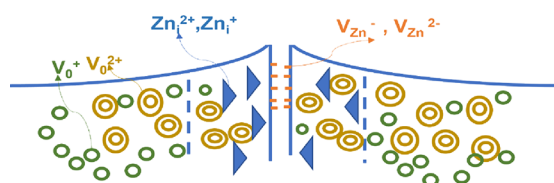
Figure 5. Proposed defect model presenting defect distribution in two semi-infinite grains sharing the same grain boundary.

predominant phase. Existence of multiphase induces the change in morphology of nanoparticles.[18,19] The synthesized samples in this study did not show any morphological change due to the multiphasic nature of the samples (the Field Effect Scanning Electron Microscopy (FE-SEM) section contains the detailed discussion). EDX measurements have confirmed the multiphase nature (Figure 1b). Existence of only Zn signal and O signal peaks clearly indicates that the extra peaks observed in the XRD pattern are due to intermediate phases (Figure 1b). We avoided chemical washing in our synthesis process to prevent from being hazardous to the environment. An interactive program on "powder diffraction data interpretation and indexing"[14] was employed to determine the lattice parameter of synthesized ZnO using XRD data. The R-factor $\sim 10^{-3}$ and $F > 10$ for all the samples are indicative of the satisfactory refinement of the lattice parameters. Figure 1c depicts the determined lattice parameters a and c as a function of synthesis temperature (T_S). The inset of the figure indicates minimum in c/a ratio at T_S = 300 °C, though the difference is negligible.

The average particle size[20] of the ZnO nanoparticles was determined (Table 1) from the Williamson−Hall plot using the intercept value from $\beta \cos \theta$ versus $4 \sin \theta$ plot (not

included here for the purpose of conciseness), as described elsewhere.[21] Here, β represents the FWHM of XRD peaks for the ZnO phase. XRD investigation has been further verified with FE-SEM findings.

3.2. Field Effect Scanning Electron Microscopy (FE-SEM). FE-SEM images (Figure 2) show the variation in shape and size of synthesized ZnO formed at different temperatures. At low temperatures, nanorods (NRs) were formed, whereas at higher temperatures ($T_S \geq 600$ °C), there was a tendency to form pseudo spheroid nanoparticles (NPs). The shape and size of the photocatalyst are some of its most conducive characteristics toward the favorable outcome of the light-driven process in water remediation. The formation of flakes at lower temperature is in agreement with Sunainea et al.[22] These authors showed sheet-like morphology having 200 μm size of zinc acetate. These sheets on calcination at different heating rates led to the formation of NRs and NPs.[22] Additionally, they reported a change in morphology of nanomaterials with variation in the heating rate, viz., NRs at a low heating rate of 40 °C/h and NPs at high heating rates of 80, 120, and 200 °C/h.[22] Deebansok et al. demonstrated a change in ZnO morphology like flakes and spheres by varying the precursor concentration during the hydrothermal synthesis process.[23] The progressive heating temperature expedites bonding between particles rendering the change in morphology from rods to spheroid. This phenomenon was reported earlier when pseudo spherical shaped ZnO nanoparticles were prepared by the direct precipitation method at 550 °C for 2 h by Chen et al.[24] While sintering the sample at 900 °C with an objective to obtain phase pure ZnO, Vijayalakshmi et al.[15] also observed changes in morphology and reported spherical structures.

The aspect ratio of the synthesized NRs was determined using the longest and distinctly observed NRs for all the
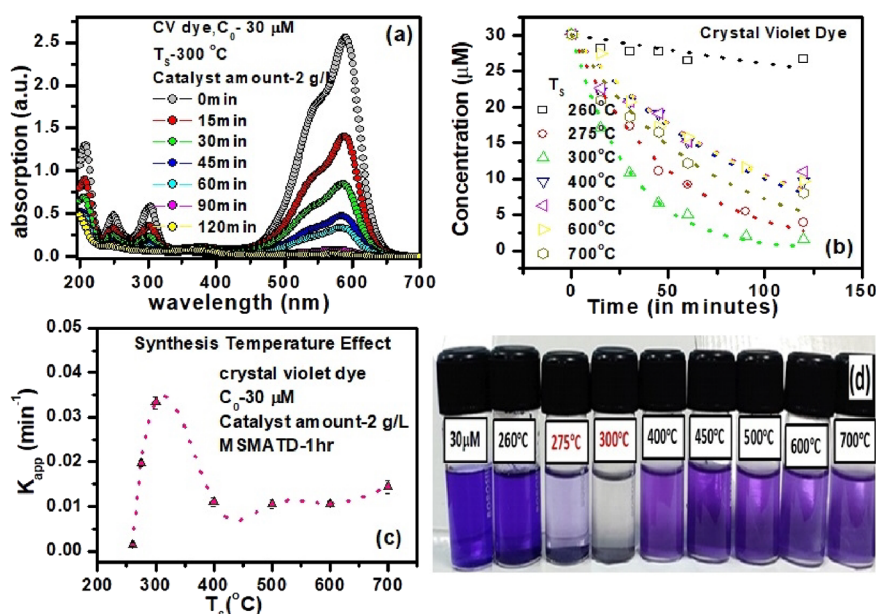
Figure 6. (a) Change in the absorption signal from the CV dye after regular interval of time for $C_O = 30\ \mu M$ and the photocatalyst amount (MSMATD synthesized ZnO) = 2 g/L; ZnO is prepared at 300 °C. (b) Pseudo first-order reaction of the CV dye under visible light exposure using ZnO synthesized at $T_S = 260-700$ °C. (c) Rate constant, K_{app}, for crystal violet dye degradation, degraded using ZnO synthesized at 300 °C and using a photocatalyst amount of 2 g/L, $C_O = 30\ \mu M$. (d) CV dye degradation with ZnO synthesized at different temperatures. $C_O = 30\ \mu M$, photocatalyst amount = 2 g/L; 10 mL of dye solution, picture taken after 120 min of exposure. For ZnO synthesized at 300 °C, $\eta = 97.30\%$ (in 120 min) and 93.18% (in 90 min).
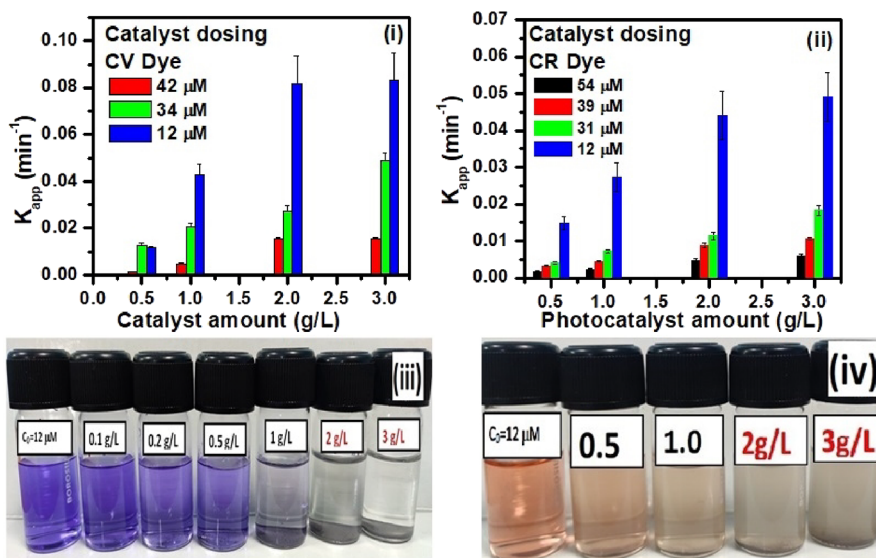
Figure 7. (i) Effect of the amount of the MSMATD synthesized ZnO photocatalyst on degradation of the CV dye at $\lambda_{max} = 587$ nm, $T_S = 300$ °C (results of some amounts are shown for the sake of clarity). (ii) Effect of the amount of the MSMATD synthesized ZnO photocatalyst on degradation of the CR dye at $\lambda_{max} = 496$ nm, $T_S = 300$ °C for various initial dye concentrations. (iii) Catalyst loading experiment: CV dye degradation with ZnO synthesized at 300 °C with different photocatalyst amounts. $C_O = 12\ \mu M$, photocatalyst amount of 0.1−3 g/L; 10 mL of dye solution, ZnO synthesized at 300 °C, picture taken after 45 min of exposure. For ZnO in 2 g/L amount, $\eta = 88.97\%$ (in 45 min) and 87.05% (in 30 min). (iv) Catalyst loading experiment: CR dye degradation with ZnO synthesized at 300 °C with different catalyst amounts. $C_O = 12\ \mu M$, photocatalyst amount of 0.5−3 g/L; 10 mL of dye solution, ZnO synthesized at 300 °C, picture taken after 25 min of exposure. For ZnO in a 2 g/L amount, $\eta = 88.6\%$ (in 25 min) and 54.78% (in 15 min).

samples synthesized at the specific temperatures (Figure 2 and Table 1). NPs synthesized at 700 °C were comparatively bigger in size as compared to NPs synthesized at 600 °C. Raoufi reported an increase in pseudo spherical nanoparticle size for ZnO prepared by the precipitation method and annealed for 4 h at 250−550 °C.[25] The particle sizes as evaluated from XRD (Table 1) are different from those

obtained from FE-SEM analysis. Such differences occur when the sample contains particles of varying sizes, and XRD analysis is known to provide average particle size. A very marginal increase in particle size with an increase in temperature from 600 to 700 °C is seen via XRD (Table 1). Thus, the NPs formed at 600 and 700 °C are not homogeneous with respect to particle size and consist of a high number of fine particles
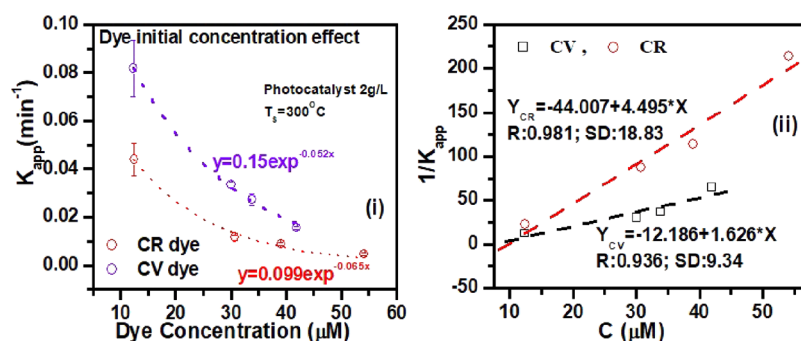
Figure 8. (i) Apparent rate constant for degradation of the CV and CR dye using ZnO NRs synthesized at 300 °C, photocatalyst amount = 2 g/L. (ii) $1/K_{app}$ vs the initial dye concentration to obtain adsorption and photocatalytic degradation of the CV and CR dye using nanorods synthesized at 300 °C, photocatalyst amount = 2 g/L.

Table 3. Kinetic Parameters of Photocatalytic Degradation of the CV and CR Dye[a]

dyes	CV	CR
R	0.936	0.981
K_O	82.17%	68.53%
K	17.82%	31.46%
$K_{app} = K_O K$ (from the L-H model)	0.08204 min^{-1}	0.0227 min^{-1}
K_{app} experimental value at $C_O = 10$ μM	0.08175 min^{-1}	0.04409 min^{-1}

[a]CV and CR are exposed to visible light under the effect of NRs synthesized at 300 °C and used 2 g/L.

along with a small number of large particles. This is also evident in FE-SEM images of the NPs formed at 600 and 700 °C (Figure 2). Also, previously reported green synthesis procedures showed non-uniform particle size growth of ZnO.[26,27]

The aspect ratio is increasing with a decrease in synthesis temperature from 500 down to 275 °C. This is in agreement with earlier report[28] showing an increase in diameter and decrease in length of nanorods while increasing calcination temperature from 350 to 450 °C during mechanical-assisted thermal decomposition of Zinc acetate dihydrate. On the other hand, Fu et al. showed the increase in the aspect ratio of ZnO NRs with an increase in the reagent concentration.[29] Thus, the morphology, particle size, and aspect ratio were found to vary

with variation in synthesis temperature (T_S). The effect on the band gap was analyzed via diffuse reflectance spectroscopy in the next section.

3.3. Diffuse Reflectance Spectroscopy (DRS). For all NPs and NRs prepared at $T_S \geq 275$ °C, a strong reflection was observed (Figure 3a) in visible range (above ~386 nm). With a decrease in synthesis temperature from 700 to 275 °C (Table 1 and Figure 3b), the absorbance peak shifted to lower wavelength. A sharp shift for ZnO prepared below $T_S = 400$ °C points to a blue shift with lowering of T_S. This visible blue shift could be due to the confinement effect. Kumar Jangir et al.[19] also reported a blue shift with lowering particle size of ZnO nanoparticles prepared by various techniques. The band gap energy of the synthesized ZnO nanoparticles and nanorods was evaluated using Kubelka−Munk (KM) relation as described earlier.[17,30−32] The intercept of the Kubelka−Munk (KM) function versus energy yielded a band gap value as shown for the sample prepared at 300 °C (Figure 3c).

The reduction in band gap (Figure 3d) of ZnO nanomaterials as compared to bulk ZnO (in 3.3 eV) could be due to zinc and oxygen vacancies, zinc and oxygen interstitials, and dislocation and stacking faults. The presence of defects in synthesized ZnO NRs and NPs was investigated via photoluminescence spectroscopy.

3.4. Photoluminescence (PL) Spectroscopy. We investigated optical properties of synthesized ZnO to understand its application as the photocatalyst in the textile dye

Table 4. Comparison of the Photocatalytic Degradation Parameter in This Work with Existing Literature for the CV and CR Dye

photocatalyst	dye	dye conc. (μM)	dye solution (mL)	photocatalyst amount (g/L)	time duration (min)	η (%)	rate const. (min^{-1})	source	ref
ZnO	CV	12.256	100	0.08	240	82	0.00739	UV, Hg vapor lamp,125 W	55
ZnO flower nanomaterial	CV	24.51		0.1	80	~96		UV, Xe arc lamp, 300 W	44
pristine ZnO	CV	24.51	100	0.05	60	40		tungsten incandescent lamp	56
ZnO	CV	~12	10	2	(i) 30 , (ii) 45	(i) 87, (ii) 89	0.08175	Hg lamp80 W	this research paper
ZnO	CR	71.77	50	0.05	50	25	0.0054	Xe lamp, 350 W	55
ZnO	CR	28.7	300	0.5	60	95.02		UV-A, 365 nm	54
ZnO@0.25Ag thin film	CR	21.54	8	thin film	120	91.9	0.0211	350 W Xe lamp	57
ZnO thin film	CR	10	40	thin film (2 cm × 2 cm)	2880	75.6		florescent lamp	58
ZnO	CR	~12	10	2	25	89	0.5535	Hg Lamp80 W	this research paper

contaminated water remediation. The nanoparticle size, defect in the crystalline structure, and surface states affect the PL properties of ZnO.[33] In general, RT PL of ZnO exhibits a sharp (UV range) and a broad transition (visible range). The sharp transition corresponds to the band-to-band transition and the broad emission is due to dopant, impurities, and/or point defects such as zinc interstitial and oxygen vacancies in the ZnO.[17,34]

The PL spectra of MSMATD synthesized ZnO NRs and NPs showed two emission peaks, one in the UV range (between 382 and 385 nm, see Table 2) and second in the visible range corresponding to defect states (Figure 4a and Table 2).

The broad peak in the visible range was reported earlier for ZnO NPs and NRs prepared using an aqueous chemical growth method,[35] wet chemical approach, and green approach (like green tea leaves).[19] In synthesized ZnO, narrow UV emission observed at 382−385 nm was due to the band-to-band transition in synthesized NRs and NPs. The narrow peak in the UV range indicates good optical properties[36] of the synthesized NRs and NPs. It is well comprehended that intrinsic defects are lesser in well-ordered grains, further enhancing the luminous efficiency of the UV band. A similar result was also concluded by Godlewski et al.,[37] demonstrating the intense edge emission from the GaN film for well-resolved grains unlike the emission from the structure-less overgrowth film. The emission spectra of the ZnO nanomaterial depend on the synthesis process.[38−42] The emission band for synthesized ZnO NRs and NPs prepared at T_S = 275−700 °C shows an asymmetric broad band in the green domain of a visible spectrum. For interpreting defect chemistry in MSMATD-synthesized NRs and NPs and their role on photocatalysis, the broad band was fitted to Gaussian peaks with a slight change in the peak position (0.05 eV). This slight change was due to the varied local environment of the defect center in different samples. Similar observations of change in the Gaussian peak position due to varied local environments were reported by Vanheusden et al.[43] and Ye et al.[36]

A higher number of fitted peaks in the PL spectra indicate the presence of various defect states (Figure 4b). The peak fitting graphs corresponding to only two synthesis temperatures are shown for conciseness (Figure 4b(i, ii)). The parameters obtained from fitted peaks, viz., peak position, FWHM, area under the curve, and relative intensities of peak, are tabulated (Table 2). Here, area under the peak was calculated, considering that the UV peak is 100%.

3.4.1. Proposed Defect Model. In the undoped ZnO, oxygen vacancies are tremendously present due to low formation enthalpy, which result in green emissions.[44] In ZnO nanomaterial, oxygen vacancies may exist in their charged state as[36] the (i) V_o^o state (oxygen vacancy, which has captured two electrons); (ii) V_o^+ (single-positive charged wrt to the lattice); and (iii) V_o^{2+} (doubly positively charged wrt to the lattice).

Band bending occurs at the grain boundaries that is crucial in terms of defect chemistry and eventually in photocatalytic efficiency. When grain boundaries have lower chemical potential than the grains, a potential barrier develops at the boundary.[45] Gupta and Carlson proposed an atomic model[46] assuming donor-like positively charged defects in the depletion layer. Close to the grain boundary, there would be a depletion region where most of oxygen vacancies were expected to be in the V_o^+ state. Band bending would create an electron depletion

region, so most of the vacancies would be in the V_o^{2+} diamagnetic state. Meanwhile, in bulk, both V_o^{2+} and V_o^+ would be higher, and their ratios would be as per synthesis temperature, with majority of the defects expected to be in the V_o^+ paramagnetic state (Figure 5). This is in agreement with the observed PL intensity (Figure 4c) for 2.1, 2.3, and 2.5 eV emissions in our experiments. At higher T_S, the synthesized ZnO nanomaterial has a globular structure of larger dimensions and thus the large grain size indicates a less surface to volume ratio. Hence, there would be more proportion of bulk as compared to the depletion region. This finding is in agreement with high observed 2.1 and 2.5 eV emissions in PL spectra (indicating higher V_o^{2+} and V_o^+ defects).

Nanorods prepared at T_S = 300 °C showed a sharp UV peak indicating well-ordered grains with lesser intrinsic defects. At T_S = 300 °C, there was possibly a reduction in barrier height due to $Zn_i^+ + V_{Zn}^- = Zn_i^0 + V_{Zn}^0$ at the grain boundary, and band bending could be ignored. A similar reduction in the barrier was proposed for ZnO varistors.[46] Consequently, due to reduced depletion width, a dip was expected in V_o^{2+} defect states and hence supported the absence of 2.1 eV peak emission in PL spectra (see Figure 4c).

3.5. Application: Textile Dye Degradation Test. Photocatalytic efficiency was evaluated against CV and CR dyes using MSMATD synthesized ZnO photocatalysts. The following equation was used to obtain degradation efficiency

$$\eta(\%) = \frac{C_o - C_t}{C_o} \times 100 \tag{1}$$

Here, C_O is the initial concentration of the dye and C_t is the concentration of the dye after photocatalytic action of ZnO after a certain duration of time.

Langmuir−Hinshelwood (L-H)[47] is the most popular kinetic model that can explain the photocatalytic degradation rate (r) of the textile dye. According to the L-H model, for mono-molecular reaction (that is photocatalytic reaction of the dye adsorbed in Langmuir's fashion)[19,48,49]

$$r = \frac{dC}{dt} = -\frac{K_O K C}{1 + K C} \tag{2}$$

where t is the reaction time, K_O is the photocatalytic reaction rate constant, K is the adsorption coefficient of the textile dye on the photocatalyst (ZnO), and C is the concentration of the dye in the bulk at equilibrium, after the dye is adsorbed by a photocatalyst obeying a Langmuir isotherm and the adsorption equilibrium is maintained during the photocatalytic reaction.

The above equation is often modified depending on the reaction condition. For a low concentration, $KC \ll 1$, the above equation gets simplified to the pseudo first-order reaction equation

$$r = \frac{dC}{dt} = -K_O K C = -K_{app} C \tag{3}$$

where K_{app} is the apparent pseudo first-order rate constant. The above equation is useful for assessing reaction kinetics when the reactant concentration (dye concentration) and adsorption coefficient or both are small. Taking integration on both sides for the above equation

$$\int \frac{dC}{C} = -K_{app} \int dt \tag{4}$$

$$\ln C + C_1 = -K_{app} t \qquad (5)$$

Applying the initial condition (at $t = 0$ s, $C = C_O$) results in[47,50,51]

$$\ln \frac{C}{C_O} = -K_{app} t \;\text{or}\; C_t = C_O e^{-K_{app} t} \qquad (6)$$

The plot of C_t versus degradation time, t, shall exhibit an exponentially decaying curve. Fitting of C_t versus t curve shall yield K_{app}.

If $KC > 1$, then eq 2 reduces to the pseudo zero-order reaction model $\frac{dC}{dt} = -K_O$, which on integration results in $C_t = C_O - K_O t$. In this case (high concentration), the concentration of the dye is expected to vary linearly with time. The parameter K_O and K can be obtained by linearizing eq 2, that is, reciprocal of eq 2

$$-\frac{1}{r} = \frac{1}{K_O K C} + \frac{1}{K_O} \qquad (7)$$

From eqs 3 and 7

$$\frac{1}{K_{app}} = \frac{1}{K_O K} + \frac{C}{K_O} \qquad (8)$$

Thus, plotting $\frac{1}{K_{app}}$ against the equilibrium concentration should be a straight line with slope $\frac{1}{K_O}$ and intercept $\frac{1}{K K_O}$.

3.5.1. Effect of Synthesis Temperature and Catalyst Dosage.

The effect of the amount of the synthesized ZnO NRs or NPs used in photocatalysis was evaluated on the CV and CR dye degradation by measuring absorption curves via UV−visible spectroscopy. The absorption peak decreased progressively with exposure time, indicating a decrease in the dye concentration in the solution due to the photocatalytic effect (Figure 6a). The exponential fitting of the concentration versus exposure time (t) plots was used to compute the apparent kinetic reaction rate constant values (Figure 6b).

The photocatalytic degradation fits the pseudo first-order reaction as discussed above and is shown in Figure 6b. The degradation profile of the CV dye under visible light exposure (Figure 6b) showed a correlation with synthesis temperature of photocatalyst nanomaterials (over T_S from 260 to 700 °C). The ZnO photocatalyst synthesized at $T_S = 300$ °C was found to be most appropriate for photocatalytic degradation (Figure 6c,d). ZnO NRs synthesized via MSMATD showed surface trap states (as discussed under the Photoluminescence (PL) Spectroscopy section; Figure 4b(iv)). The active surface traps led to delayed recombination time, which enhanced photocatalytic efficiency.

After finding the optimum synthesis temperature of the photocatalyst, the effect of the photocatalyst amount was investigated for CV and CR dyes (Figure 7(i,ii)). The decolorizing efficiencies generally improves upon increasing the amount of the photocatalyst to an optimum amount for a certain illumination time.[52] The optimized dosage facilitates not only the best degradation efficiencies[53] but also its cost effectiveness.

Our findings suggested that the rate constant (K_{app}) is influenced by the ZnO amount. Initially, there was an increase in the rate constant with an increase in dose due to the proportional increase in the photocatalytic sites generating more radicals. The ZnO photocatalyst per liter of dye solution (2 g) was optimum dose (Figure 7(i−iv)) to achieve the highest CV and CR degradation with the MSMATD synthesized ZnO photocatalyst. Further, an increase in dose showed saturation in the rate constant. This could be due to the blockage of photocatalytic activity of one NR by another. In the existing work, any rotation, shaking, or stirring was not undertaken during the photocatalytic test. Shaking or stirring during the photocatalytic test will be taken in extended work.

It is worth mentioning that decolouration is not the confirmation of complete mineralization of the dye. Other analytical characterizations like chromatographic techniques were not in the scope of this study and may be undertaken during subsequent research work.

3.5.2. Effect of the CV and CR Dye Concentration.

The impact of the initial dye concentration on photocatalytic degradation of the CV and CR dye was investigated by varying the initial dye concentration over a wide range. Photocatalytic performance of synthesized NRs was inversely proportional to the initial dye concentration under the same experimental conditions (Figure 8(i)). For the CV and CR dye, the apparent rate constant with the initial concentration was seen to decay exponentially. For the CR dye, the apparent rate constant initially decreased sharply with an increase in the concentration and led to saturation. Interestingly, 30 μM onward, the CV dye showed a faster decrease in K_{app}, and for the CR dye, it was already low (Figure 8(i)). This abatement (for the CR dye) could be due to the decreased absorption of photons on the photocatalyst surface owing to the increased dye concentration or adsorption on the catalyst surface, which in turn reduced radicals' generation.

3.5.3. Effect Rate Constant and Adsorption Coefficient.

Figure 8(i) is replotted as $1/K_{app}$ versus the initial dye concentration to obtain the adsorption and photocatalytic degradation contributions (Figure 8(ii)); $1/K_{app}$ versus the initial dye concentration yielded a line with high correlation coefficients, $R = 0.9811$ and 0.936 for CR and CV dyes, respectively. The photocatalytic reaction rate constant, K_O, and adsorption coefficient of the textile dye on ZnO NR were determined from the slope ($= 1/K_O$) and intercept ($= 1/K_O K$), respectively. The values of K_O and K were 0.615 μM/min and 0.1334 1/μM, respectively (for the CV dye), and 0.2224 μM/min and 0.1021 1/μM, respectively (for the CR dye).

Table 3 shows the kinetic parameters of photocatalytic degradation of CV and CR dyes. The product $K_O K = K_{app}$ for CV was obtained as 0.082 min^{-1} and matched exactly (% difference = 0.35%) with the experimental K_{app} value (= 0.0817 min^{-1}) at 10 μM, indicating that photocatalytic degradation can be satisfactorily described by the L-H model for the CV dye. However, for the CR dye, the product $K_O K = K_{app}$ is 0.0227, which was different than the experimentally obtained value of $K_{app} = 0.04409$ min^{-1} (% difference = 94.22%). The correlation coefficient is greater than 0.9 indicating validity of the fit, but there is high difference in K_{app} values obtained from the L-H model and the experimental results. This suggests that the L-H model would not be suitable to describe photocatalytic CR dye degradation using MSMATD synthesized ZnO nanomaterials. On the other hand, the photocatalytic CV dye degradation using MSMATD synthesized ZnO is satisfactorily explained by the L-H kinetic model over a wide range of CV dye concentrations. This finding is in agreement with Elaziouti and Ahmed whose study on CR dye degradation concluded the L-H model to be inappropriate for explaining photocatalytic degradation using commercially obtained ZnO.[54] Based on our results, we propose MSMATD

synthesized NRs prepared at 300 °C as the best for photocatalytically degrading the CV and CR dye in the smallest time. Existing photocatalytic research work on CV and CR utilizing ZnO is presented in Table 4 for comparison.

4. CONCLUSIONS

An improved, environment friendly methodology has been established to obtain high efficiency ZnO photocatalyst nanorods. Photocatalysis rate strongly depends on defect occurrence and thus on the synthesis process and parameters. ZnO nanorods synthesized via magnetic stirred mechanical-assisted thermal decomposition at 300 °C exhibited the highest photocatalysis efficiency against crystal violet and congo red dyes. The degradation kinetics of both dyes are fast with 87 and 89% efficiencies in 30 and 25 min for the CV and CR dye, respectively. Moreover, the comparison with previous studies clearly indicates the better degradation in terms of degradation time with low energy consumption. Photocatalytic degradation of the crystal violet dye obeyed the Langmuir–Hinshelwood model unlike the congo red dye. Defect occurrences have been correlated with the photocatalytic efficiency of pristine ZnO. A defect model based on morphological and photoluminescence investigations has been proposed for the synthesized ZnO.

■ AUTHOR INFORMATION

Corresponding Author

　Suchitra Rajput Chauhan − *Centre for Advanced Materials and Devices (CAMD), School of Engineering and Technology, BML Munjal University, Gurgaon 122413 Haryana, India;* ⊙ orcid.org/0000-0003-1782-3102; Phone: 91-120-4806860; Email: suchitra.rajput.chauhan@ iitdalumni.com, rajput.suchitra@gmail.com; Fax: 91-120-480688

Authors

　Sumit Kumar − *Centre for Advanced Materials and Devices (CAMD), School of Engineering and Technology, BML Munjal University, Gurgaon 122413 Haryana, India*

　Jyoti Pandey − *Centre for Advanced Materials and Devices (CAMD), School of Engineering and Technology, BML Munjal University, Gurgaon 122413 Haryana, India*

　Ritika Tripathi − *Centre for Advanced Materials and Devices (CAMD), School of Engineering and Technology, BML Munjal University, Gurgaon 122413 Haryana, India*

Complete contact information is available at:
https://pubs.acs.org/10.1021/acsomega.3c03860

Author Contributions

S.R.C. performed the experiments, data analysis, conceptualization, funding acquisition, writing of the original draft, review, editing, and supervision; J.P. performed the XRD result evaluation and documentation; R.T. performed the FE-SEM analysis and documentation; S.K. performed the PL measurement, literature tables, and documentation. All authors have read and agreed to the published version of the manuscript.

Notes

The authors declare no competing financial interest.

■ ACKNOWLEDGMENTS

■ REFERENCES

(1) Lisa, Guppy, Kelsey, Anderson. (2017) *Global Water Crisis: The Facts*; Hamilton, Canada.

(2) Anshu, A.; Vijayaraghavan, R. Metal peroxide- polymer composites for dye degradation. *IOP Conf. Ser. Mater. Sci. Eng.* **2017**, *263*, No. 022007.

(3) Alinsafi, A.; Khemis, M.; Pons, M. N.; Leclerc, J. P.; Yaacoubi, A.; Benhammou, A.; Nejmeddine, A. Electro-coagulation of reactive textile dyes and textile wastewater. *Chem. Eng. Process.: Process Intesif.* **2005**, *44*, 461−470.

(4) Métivier-Pignon, H.; Faur-Brasquet, C.; Le Cloirec, P.; Jaouen, P. Coupling ultrafiltration with an activated carbon cloth for the treatment of highly coloured wastewaters : A techno-economic study. *Environ.Technol.* **2003**, *24*, 735−743.

(5) Pirhashemi, M.; Habibi-Yangjeh, A.; Rahim Pouran, S. Review on the criteria anticipated for the fabrication of highly efficient ZnO-based visible-light-driven photocatalysts. *J. Ind. Eng. Chem.* **2018**, *62*, 1−25.

(6) Zhang, Y. C.; Du, Z. N.; Zhang, M. Hydrothermal synthesis of SnO2/SnS2 nanocomposite with high visible light-driven photocatalytic activity. *Mater. Lett.* **2011**, *65*, 2891−2894.

(7) Malhotra, A.; Mutton, G.; Chauhan, S. R.; Semetey, V.; Chauhan, A. Medical device associated-biofilm eradication strategies. *Appl. Multifunct. Nanomater.* **2023**, 595−616.

(8) Fresno, F.; Portela, R.; Suárez, S.; Coronado, J. M. Photocatalytic materials: Recent achievements and near future trends. *J. Mater. Chem. A Mater.* **2014**, *2*, 2863−2884.

(9) Kayaci, F.; Vempati, S.; Ozgit-Akgun, C.; Donmez, I.; Biyikli, N.; Uyar, T. Transformation of polymer-ZnO core-shell nanofibers into ZnO hollow nanofibers: Intrinsic defect reorganization in ZnO and its influence on the photocatalysis. *Appl. Catal. B* **2015**, *176-177*, 646−653.

(10) Zhu, Y.-P.; Ren, T.-Z.; Yuan, Z.-Y. Mesoporous phosphorus-doped g-C 3 N 4 nanostructured flowers with superior photocatalytic hydrogen evolution performance. *ACS Appl. Mater. Interfaces* **2015**, *7*, 16850−16856.

(11) Naldoni, A.; Allieta, M.; Santangelo, S.; Marelli, M.; Fabbri, F.; Cappelli, S.; Bianchi, C. L.; Psaro, R.; Dal Santo, V. Effect of nature and location of defects on bandgap narrowing in black TiO 2 nanoparticles. *J. Am. Chem. Soc.* **2012**, *134*, 7600−7603.

(12) Özgür, Ü.; Alivov, Y. I.; Liu, C.; Teke, A.; Reshchikov, M. A.; Doğan, S.; Avrutin, V.; Cho, S. J.; Morkọ, H. A comprehensive review of ZnO materials and devices. *J. Appl. Phys.* **2005**, *98*.

(13) Rajendran, S.; Khan, M. M.; Gracia, F.; Qin, J.; Gupta, V. K.; Arumainathan, S. Ce3+−ion-induced visible-light photocatalytic degradation and electrochemical activity of ZnO/CeO2 nanocomposite. *Sci. Rep.* **2016**, *6*.

(14) Wu, B. E. (1978) *POWD, an interactive program for powder diffraction data interpretation and indexing*. Program Complex FROG. Software, iss.

(15) Vijayalakshmi, U.; Chellappa, M.; Anjaneyulu, U.; Manivasagam, G.; Sethu, S. Influence of Coating Parameter and Sintering Atmosphere on the Corrosion Resistance Behavior of Electrophoretically Deposited Composite Coatings. *Mater. Manuf. Processes* **2016**, *31*, 95−106.

(16) Luković Golić, D.; Branković, G.; Počuča Nešić, M.; Vojisavljević, K.; Rečnik, A.; Daneu, N.; Bernik, S.; Šćepanović, M.; Poleti, D.; Branković, Z. Structural characterization of self-assembled ZnO nanoparticles obtained by the sol-gel method from Zn-(CH3COO)2 2H2O. *Nanotechnology* **2011**, *22*, No. 395603.

(17) Malhotra, A.; Rajput Chauhan, S.; Rahaman, M.; Tripathi, R.; Khanuja, M.; Chauhan, A.; Ghosh, S.; Satriano, C.; Turner, R. J. Phyto-assisted synthesis of zinc oxide nanoparticles for developing

antibiofilm surface coatings on central venous catheters. *Front. Chem.* **2023**, *11*, 1−12.

(18) Qian, F.; Lan, P. C.; Olson, T.; Zhu, C.; Duoss, E. B.; Spadaccini, C. M.; Han, T. Y. J. Multiphase separation of copper nanowires. *Chem. Commun.* **2016**, *52*, 11627−11630.

(19) Kumar Jangir, L.; Kumari, Y.; Kumar, A.; Kumar, M.; Awasthi, K. Investigation of luminescence and structural properties of ZnO nanoparticles, synthesized with different precursors. *Mater. Chem. Front.* **2017**, *1*, 1413−1421.

(20) Cullity, B. D., Bernard, D. (1978) *Elements of x-ray diffraction.* Addison-Wesley Publishing Company, Inc.

(21) Chauhan, S. R.; Chaudhary, S. On the residual resistivity ratio in MgB2 superconductors. *IEEE Trans. Appl. Supercond.* **2010**, *20*, 26−32.

(22) Sunainea; Sreekanth, M.; Ghosh, S.; Mehta, S. K.; Ganguli, A. K.; Jha, M. Investigation of the growth mechanism of the formation of ZnO nanorods by thermal decomposition of zinc acetate and their field emission properties. *CrystEngComm* **2017**, *19*, 2264−2270.

(23) Deebansok, S.; Amornsakchai, T.; Sae-Ear, P.; Siriphannon, P.; Smith, S. M. Sphere-like and flake-like ZnO immobilized on pineapple leaf fibers as easy-to-recover photocatalyst for the degradation of congo red. *J. Environ. Chem. Eng.* **2021**, *9*, No. 104746.

(24) Chen, C. C.; Liu, P.; Lu, C. H. Synthesis and characterization of nano-sized ZnO powders by direct precipitation method. *Chem. Eng. J.* **2008**, *144*, 509−513.

(25) Raoufi, D. Synthesis and photoluminescence characterization of ZnO nanoparticles. *J. Lumin.* **2013**, *134*, 213−219.

(26) Priyadharshini, S. S.; Shubha, J. P.; Shivalingappa, J.; Adil, S. F.; Kuniyil, M.; Hatshan, M. R.; Shaik, B.; Kavalli, K. Photocatalytic Degradation of Methylene Blue and Metanil Yellow Dyes Using Green Synthesized Zinc Oxide (ZnO) Nanocrystals. *Crystals (Basel)* **2022**, *12*, 22.

(27) Azizi, S.; Mohamad, R.; Mahdavi Shahri, M. Green Microwave-Assisted Combustion Synthesis of Zinc Oxide Nanoparticles with Citrullus colocynthis (L.) Schrad: Characterization and Biomedical Applications. *Molecules* **2017**, *22*.

(28) Zhang, X.; Qin, J.; Xue, Y.; Yu, P.; Zhang, B.; Wang, L.; Liu, R. Effect of aspect ratio and surface defects on the photocatalytic activity of ZnO nanorods. *Sci. Rep.* **2014**, *4*.

(29) Fu, D.; Han, G.; Meng, C. Size-controlled synthesis and photocatalytic degradation properties of nano-sized ZnO nanorods. *Mater. Lett.* **2012**, *72*, 53−56.

(30) Wetchakun, N.; Chaiwichain, S.; Inceesungvorn, B.; Pingmuang, K.; Phanichphant, S.; Minett, A. I.; Chen, J. BiVO 4/CeO 2 nanocomposites with high visible-light-induced photocatalytic activity. *ACS Appl. Mater. Interfaces* **2012**, *4*, 3718−3723.

(31) Zhang, Z.; Wang, W.; Wang, L.; Sun, S. Enhancement of visible-light photocatalysis by coupling with narrow-band-gap semiconductor: A case study on Bi 2S 3/Bi 2WO 6. *ACS Appl. Mater. Interfaces* **2012**, *4*, 593−597.

(32) Tauc, S. J. OPTICAL PROPERTIES AND ELECTRONIC STRUCTURE OF AMORPHOUS GE AND SI. *Mat. Res. Bull.* **1968**, *3*, 37−46.

(33) Chestnoy, N.; Harris, T. D.; Hull, R.; Bruss, L. E. Luminescence and Photophysics of CdS Semiconductor Clusters: The Nature of the Emitting Electronic State. *J. Phys. Chem.* **1985**, *90*, 3393−3399.

(34) Vempati, S.; Mitra, J.; Dawson, P. One-step synthesis of ZnO nanosheets: A blue-white fluorophore. *Nanoscale Res. Lett.* **2012**, *7*.

(35) Zhao, J. H.; Liu, C. J.; Lv, Z. H. Photoluminescence of ZnO nanoparticles and nanorods. *Optik (Stuttg)* **2016**, *127*, 1421−1423.

(36) Ye, J. D.; Gu, S. L.; Qin, F.; Zhu, S. M.; Liu, S. M.; Zhou, X.; Liu, W.; Hu, L. Q.; Zhang, R.; Shi, Y.; Zheng, Y. D. Correlation between green luminescence and morphology evolution of ZnO films. *Appl. Phys. A: Mater. Sci. Process.* **2005**, *81*, 759−762.

(37) Godlewski, M.; Goldys, E. M.; Phillips, M. R.; Langer, R.; Barski, A. Cathodoluminescence depth-profiling studies of GaN/AlGaN quantum-well structures. *J. Mater. Res.* **2000**, *15*, 495−501.

(38) Chen, Y. Q.; Jiang, J.; He, Z. Y.; Su, Y.; Cai, D.; Chen, L. Growth mechanism and characterization of ZnO microbelts and self-assembled microcombs. *Mater. Lett.* **2005**, *59*, 3280−3283.

(39) Meng, X. Q.; Shen, D. Z.; Zhang, J. Y.; Zhao, D. X.; Lu, Y. M.; Dong, L.; Zhang, Z. Z.; Liu, Y. C.; Fan, X. W. The structural and optical properties of ZnO nanorod arrays. *Solid State Commun.* **2005**, *135*, 179−182.

(40) Yang, Q.; Tang, K.; Zuo, J.; Qian, Y. Synthesis and luminescent property of single-crystal ZnO nanobelts by a simple low temperature evaporation route. *Appl. Phys. A: Mater. Sci. Process.* **2004**, *79*, 1847−1851.

(41) Ng, H. T.; Chen, B.; Li, J.; Han, J.; Meyyappan, M.; Wu, J.; Li, S. X.; Haller, E. E. Optical properties of single-crystalline ZnO nanowires onm-sapphire. *Appl. Phys. Lett.* **2003**, *82*, 2023−2025.

(42) Chen, Z.; Wu, N.; Shan, Z.; Zhao, M.; Li, S.; Jiang, C. B.; Chyu, M. K.; Mao, S. X. Effect of N 2 flow rate on morphology and structure of ZnO nanocrystals synthesized via vapor deposition. *Scr. Mater.* **2005**, *52*, 63−67.

(43) Vanheusden, K.; Warren, W. L.; Seager, C. H.; Tallant, D. R.; Voigt, J. A.; Gnade, B. E. Mechanisms behind green photo-luminescence in ZnO phosphor powders. *J. Appl. Phys.* **1996**, *79*, 7983−7990.

(44) Leiter, F. H.; Alves, H. R.; Hofstaetter, A.; Hofmann, D. M.; Meyer, B. K. The Oxygen Vacancy as the Origin of a Green Emission in Undoped ZnO. *Phys. Status Solidi B* **2001**, *226*, R4−R5.

(45) Seager, C. H.; Castner, T. G. Zero-bias resistance of grain boundaries in neutron-transmutation-doped polycrystalline silicon. *J. Appl. Phys.* **1978**, *49*, 3879−3889.

(46) Gupta, T. K.; Carlson, W. G. A grain-boundary defect model for instability/stability of a ZnO varistor. *J. Mater. Sci.* **1985**, 3487.

(47) Choo, K. H. (2018) Modeling Photocatalytic Membrane Reactors, in *Current Trends and Future Developments on (Bio-) Membranes: Photocatalytic Membranes and Photocatalytic Membrane Reactors*, pp. 297−316. Elsevier Inc..

(48) Ohtani, B. Photocatalysis by inorganic solid materials: Revisiting its definition, concepts, and experimental procedures. *Adv. Inorg. Chem.* **2011**, DOI: 10.1016/B978-0-12-385904-4.00001-9.

(49) Crittenden, J. C.; Liu, J.; Hand, D. W.; Perram, D. L. PHOTOCATALYTIC OXIDATION OF CHLORINATED HY-DROCARBONS IN WATER. *Water. Res.* **1997**, 429−438.

(50) Ali, S. M., Usman. (2012) *Fabrication and characterization of ZnO nanostructures for sensing and photonic device applications.* Linkoping University of Technology, Norrkoping, Sweden.

(51) Konstantinou, I. K.; Albanis, T. A. Photocatalytic trans-formation of pesticides in aqueous titanium dioxide suspensions using artificial and solar light: intermediates and degradation pathways. *Appl. Catal., B* **2003**, *42*, 319−335.

(52) Liu, Y.; Zhang, Y. C.; Xu, X. F. Hydrothermal synthesis and photocatalytic activity of CdO2 nanocrystals. *J. Hazard. Mater.* **2009**, *163*, 1310−1314.

(53) Ge, T.; Shen, L.; Li, J.; Zhang, Y.; Zhang, Y. Morphology-controlled hydrothermal synthesis and photocatalytic Cr(VI) reduction properties of α-Fe2O3. *Colloids Surf., A* **2022**, *635*, No. 128069.

(54) Elaziouti, A.; Ahmed, B. ZnO-Assisted Photocatalytic Degradation of Congo Red and Benzopurpurine 4B in Aqueous Solution. *J. Chem. Eng. Process Technol.* **2011**, *02*, 1−9.

(55) Hitkari, G.; Chowdhary, P.; Kumar, V.; Singh, S.; Motghare, A. Potential of Copper-Zinc Oxide nanocomposite for photocatalytic degradation of congo red dye. *Cleaner Chem. Eng.* **2022**, *1*, No. 100003.

(56) Dhanalakshmi, M.; Saravanakumar, K.; Prabavathi, S. L.; Muthuraj, V. Iridium doped ZnO nanocomposites: Synergistic effect induced photocatalytic degradation of methylene blue and crystal violet. *Inorg. Chem. Commun.* **2020**, *111*, No. 107601.

(57) Liu, J.; Li, J.; Wei, F.; Zhao, X.; Su, Y.; Han, X. Ag-ZnO Submicrometer Rod Arrays for High-Efficiency Photocatalytic Degradation of Congo Red and Disinfection. *ACS Sustainable Chem. Eng.* **2019**, *7*, 11258−11266.

(58) Wang, Y.; Cai, X.; Han, B.; Deng, S.; Wang, Y.; Dong, C.; Djerdj, I. Hydrothermal growth of ZnO nanorods on Zn substrates and their application in degradation of azo dyes under ambient conditions. *CrystEngComm* **2014**, *16*, 7761−7770.